







RESEARCH ARTICLE | JUNE 01 2023

Design optimization and flow analysis of discrete tip injection in a transonic compressor based on nonlinear harmonic method and endwall blockage attenuation

Wang Xuesong (王雪松) ; Sun Jinju (孙金菊)  ; Ernesto Benini ; Song Peng (宋鹏) ; Chen Wenzhuo (陈文卓) 



Physics of Fluids 35, 066103 (2023)

<https://doi.org/10.1063/5.0152319>



View
Online



Export
Citation

CrossMark

Design optimization and flow analysis of discrete tip injection in a transonic compressor based on nonlinear harmonic method and endwall blockage attenuation

Cite as: Phys. Fluids **35**, 066103 (2023); doi: 10.1063/5.0152319

Submitted: 29 March 2023 · Accepted: 15 May 2023 ·

Published Online: 1 June 2023



View Online



Export Citation



CrossMark

Xuesong Wang (王雪松),¹ Jinju Sun (孙金菊),^{1,a)} Ernesto Benini,² Peng Song (宋鹏),¹ and Wenzhuo Chen (陈文卓)¹

AFFILIATIONS

¹School of Energy and Power Engineering, Xi'an Jiaotong University, 28 West Xianning Road, 710049 Xi'an, China

²Department of Industrial Engineering, University of Padova, Via Venezia 1, 35131 Padova, Italy

^{a)} Author to whom correspondence should be addressed: jjsun@mail.xjtu.edu.cn

ABSTRACT

Discrete tip injection (DTI) shows great promise for improving the operating stability of transonic axial flow compressor (AFC) rotors. However, the design optimization of DTI remains a challenging task because of both the reliance on computationally expensive unsteady simulations to calculate its effects and the lack of a flow physics-based index for assessing operating stability. The present study introduces a nonlinear harmonic method for the rapid simulation of the dominant unsteady effects caused by a DTI device, and it proposes the unsteady shroud endwall blockage attenuation as an operating stability optimization index for DTI design based on analyzing the stall flow mechanism in transonic AFCs. On this basis, an efficient optimization method for DTI design is proposed in combination with an adaptive kriging-based optimization technique. This design optimization method is validated by the Coandă injector design for the transonic rotor National Aeronautics and Space Administration Rotor 37, with improved operating range and reduced injection mass flow pursued simultaneously by a comprehensive objective function. The optimal DTI design significantly reduces the stalling flow coefficient of the compressor by 4.46% at a small injection mass flow (0.72% of the compressor stalling mass flow), with a slight increase in the aerodynamic performance of the compressor. Detailed unsteady flow-field analysis shows that the main reason for the improved operating stability of the transonic AFC is a significant attenuation and delayed recovery of shroud endwall blockage, and the underlying flow mechanism is elucidated well.

Published under an exclusive license by AIP Publishing. <https://doi.org/10.1063/5.0152319>

NOMENCLATURE

a	distance between injector and blade leading edge	DTI	discrete tip injection
AFC	axial flow compressor	h	height of the injector outlet
B	blockage factor	LE	leading edge
B_{ave}	average shroud endwall blockage	m_{inj}	injection mass flow rate
$B_{t,max}$	maximum shroud endwall blockage near blade trailing edge	m_{NS}	compressor mass flow rate at near-stall
C	weight coefficient of objective parameter	NASA	National Aeronautics and Space Administration
Choked	choke point	NLH	nonlinear harmonic method
C_{ax}	tip axial chord length	NS	near-stall point
de_1	eccentric distance in radial direction	N_d	number of blades of the downstream row
de_2	eccentric distance in axial direction	N_H	number of harmonics
DE	design point	N_u	number of blades of the upstream row
		O_1	circle center of the inner circular arc
		O_2	circle center of the outer circular arc
		PE	peak efficiency point

P_s	static pressure
P_t	total pressure
r_1	radius of the inner circular arc
r_2	radius of the outer circular arc
R_h	radius of hub endwall
R_s	radius of shroud endwall
SEB	shroud endwall blockage
SMI	stall margin improvement
TLF	tip leakage flow
TLV	tip leakage vortex
Tt	total temperature
V	absolute velocity
V_{inlet}	average velocity at compressor inlet
W	relative velocity
W_z	axial velocity component
δ_e	local displacement thickness
Δ	relative difference of parameters
η	adiabatic efficiency
θ	circumferential width of the injector
π^*	total pressure ratio
ρ	density
τ	tip clearance size
φ	mass flow coefficient

I. INTRODUCTION

The design of axial flow compressors (AFCs) in modern aero-engines has targeted higher stage loading to reduce their number of stages, size and weight, but high-loading designs are always accompanied by some negative effects.^{1,2} One of the most serious downsides is the narrowing of the stable operating range, which not only poses a serious threat to flight safety but also leads to difficulties in stage matching and, thus, affects the operating efficiency of aero-engines. Therefore, there has been a fairly constant effort over the past few decades to develop robust stability-enhancement techniques for highly loaded AFCs.

Various passive and active techniques have been presented and researched for enhancing AFC operating stability, such as 3D blade designs,^{3–5} casing treatments,^{6–8} pitching inlet guide vanes,^{9,10} and tip injections.^{11,12} For tip-critical rotors, discrete tip injection (DTI) has been investigated extensively because it has shown significant benefits in terms of enhanced stability and lower accompanying compressor efficiency losses. The DTI air supply can be either an external air source¹³ or bled from the high-pressure region of the AFC rear part,¹⁴ but both forms of air supply require additional work for the injected flow and inevitably subject the entire system to cycle penalty. Therefore, a major focus of previous research has been on designing the DTI to maximize the stable operating range at the smallest possible injection mass flow rate and analyzing the underlying flow mechanisms of stall margin improvement (SMI).

Most previous studies of DTI design have been based on parametric research methods to investigate how injection parameters affect SMI, with the expectation of summarizing some valuable design guidelines. For example, Suder *et al.*¹¹ performed experimental and numerical studies of DTI design in a transonic AFC rotor; they subjected injection parameters including injector number, circumferential distribution of injectors, and injection flow velocity to parametric investigation, concluding that SMI is related to the total circumferential

coverage of the injectors and has nothing to do with their circumferential distribution. Cassina *et al.*¹⁵ conducted numerical simulations of DTI in an AFC stage to investigate parametrically the effects of different injection parameters, including injector aspect ratio, injection flow angle, injection mass flow rate, and axial distance between injector and blade leading edge (LE); they concluded that there is an optimal injector aspect ratio for maximum SMI with constant injection area and mass flow rate. Wang *et al.*^{13,16} studied the effects of injector throat height and circumferential coverage on SMI for a transonic and a subsonic AFC rotor; they found that the effects of these two parameters were basically the same for the two compressors when the ratio of injection velocity to mainstream velocity reached two.

Based on considerable efforts in parametric studies of DTI design, design guidelines for some of the injection parameters have become consensus. For example, for a given DTI design, a larger SMI can be achieved as the injection mass flow rate increases.^{11,15} However, systematic and universally applicable guidelines for DTI design are still difficult to establish. The reasons behind this are that, on the one hand, there are many injection parameters affecting the SMI effect of DTI design,¹⁷ and parametric studies tend to investigate the effects of several of them one by one and do not consider the cross-influence between parameters.¹⁶ On the other hand, some design guidelines exhibit obvious compressor dependence, that is, the influence pattern of some injection parameters is not consistent across AFCs. For example, based on the respective AFCs studied, Hiller *et al.*¹⁸ found that SMI could be achieved only when the injection flow exceeded 2% of the compressor flow, while the study results conducted by Wang *et al.*¹⁶ showed that significant SMI could be achieved even at an injection flow of less than 1% of the compressor flow; The results of Suder *et al.*¹¹ showed that the non-uniform distribution of injectors in the circumferential direction had no effect on SMI; however, the opposite results were obtained by Nie *et al.*¹⁹ Some studies suggested that air should be injected along the axial direction,^{11,20,21} while some others found that air is better injected along the blade camber line at the LE.^{14,15}

In addition, there are some other obvious disadvantages of parametric studies. Some design guidelines can only indicate the general direction of the DTI design, while the optimal values of the parameters still need to be further studied based on the compressor under study.¹⁷ Existing parametric studies have mainly focused on considering the SMI effect of DTI design, and it is difficult to achieve the collaborative design optimization with other objectives, such as improving compressor aerodynamic performance while achieving SMI maximization. In pursuit of greater improvements in stall margin and aerodynamic performance of AFCs, a variety of new types of injection designs are emerging,^{22,23} which pose significant challenges to the applicability of these established design guidelines. Therefore, there is an urgent need to develop an efficient and robust DTI design methodology.

Combining computational fluid dynamics (CFD) and advanced optimization techniques for the design optimization of turbomachinery is now a well-established and promising method, which can well overcome the shortcomings of parametric research methods mentioned above. To date, there are many studies on the design optimization of blades^{24–26} and casing treatments,^{27–29} but few studies have focused on the optimization of DTI designs. The reasons behind this are (i) during the process of CFD-based design optimization, a large number of new designs need to be numerically simulated; (ii) because of the DTI influence, there are significant unsteady flow phenomena

in the compressor (especially in the blade tip region), for which the numerical solutions rely on computationally expensive unsteady simulation methods; and (iii) accurate SMI calculation for an AFC with different DTI designs relies on time-consuming simulation of the complete compressor performance map. These factors make it extremely tricky and time-consuming to adopt existing optimization methods directly for DTI design optimization.

In order to better apply CFD-based design optimization methods to DTI designs, this paper develops an efficient DTI design framework. This design framework enables rapid completion of complex DTI designs, and it is easy to consider the collaborative optimization of multiple objectives. The main contributions of this paper are as follows:

- (1) To overcome the time-consuming problem of traditional time-accurate unsteady methods, a nonlinear harmonic (NLH) method is introduced to calculate rapidly the unsteady influence of DTI on the AFC performance and internal flow fields;
- (2) To avoid the time-consuming simulation of the complete compressor performance map for each new DTI design, a physics-based index for the stall margin optimization of DTI design is developed based on the analysis of the flow mechanisms in transonic AFCs;
- (3) To reduce the number of CFD calls during the DTI design optimization, an adaptive kriging-based optimization technique is used to search efficiently for the optimal solution, and a DTI design framework is established by integrating the optimization technique, NLH method, and physics-based SMI optimization index.
- (4) A Coandă injector design for the NASA Rotor 37 is implemented to validate the performance of the established design framework, in which the maximum SMI and the minimum injection mass flow rate are pursued simultaneously. Detailed performance analysis and unsteady flow interaction analysis between the rotor and optimal discrete injectors are performed using the NLH method for better physical understanding of the mechanism of DTI improving the stable operating range of the compressor.

The main contents of the paper are arranged as follows: Sec. II introduces the NLH method and its validation; Sec. III gives the DTI design framework and highlights the development of physics-based SMI optimization strategy; Sec. IV is the results discussion, including the design optimization results and the mechanism analysis of compressor operating stability enhancement; Sec. V summarizes the research of this paper.

II. NUMERICAL METHOD AND VALIDATION

A. Nonlinear harmonic method

For periodic unsteady flows such as those considered herein, the NLH method proposed by He and Ning³⁰ and Chen *et al.*³¹ can be used for rapid modeling of the dominant unsteady flow physics. A brief introduction of the NLH method is as follows.

The integral form of the unsteady Reynolds-averaged Navier–Stokes (RANS) equations in Cartesian coordinates (x, y, z) is

$$\frac{\partial}{\partial t} \int_{\Omega} U d\Omega + \int_S \vec{F}_I \cdot d\vec{S} + \int_S \vec{F}_V \cdot d\vec{S} = \int_{\Omega} S_T d\Omega, \quad (1)$$

where S is the surface; Ω is the volume of the flow domain under consideration; $U = (\rho, \rho\vec{v}, \rho E)$ is the conservative variable; \vec{F}_I and \vec{F}_V

are the inviscid and viscous flux vectors, respectively; and S_T is the source term.

The main idea behind the NLH method is to decompose the unsteady conservative flow variable within a computational domain at location \vec{r} and time t into the sum of a time-averaged variable \bar{U} and periodic perturbations U' , that is,

$$U(\vec{r}, t) = \bar{U}(\vec{r}) + \sum U'(\vec{r}, t). \quad (2)$$

Furthermore, each periodic perturbation U' can be represented as a Fourier decomposition of a finite number of time harmonics, that is,

$$U'(\vec{r}, t) = \sum_{k=1}^{N_H} (\tilde{U}_k(\vec{r})e^{i\omega_k t} + \tilde{U}_{-k}(\vec{r})e^{-i\omega_k t}), \quad (3)$$

where N_H is the number of time harmonics, \tilde{U}_k and \tilde{U}_{-k} are the complex-conjugate amplitudes of the k th time harmonic, and ω_k is its angular frequency.

Then, analogously to Reynolds averaging (the difference here being that the perturbation is periodic), the time-averaged flow equations are obtained and can be written as

$$\Omega_i \left(\frac{d\bar{U}}{dt} \right)_i = - \sum_{\text{cellfaces}} \bar{F}_C \bar{S} + \sum_{\text{cellfaces}} \bar{F}_V \bar{S} + \Omega_i \bar{S}_{Ti}, \quad (4)$$

where i refers to cell i , Ω_i is its volume, and \bar{F}_C and \bar{F}_V are the discretized convective and viscous fluxes, respectively.

At the same time, deterministic stress terms are introduced into the time-averaged equations because of the nonlinearity, just like the Reynolds stress terms that appear in the Reynolds-averaged equations. Therefore, the convective and viscous flux terms in the flow control equations should contain the contributions of the deterministic stress terms, that is,

$$\bar{F}_C \bar{S} = \begin{bmatrix} (\bar{\rho}\vec{v} \cdot \bar{S}) \\ (\bar{\rho}\vec{v} \cdot \bar{S})\bar{v}_x + \bar{p}S_x \\ (\bar{\rho}\vec{v} \cdot \bar{S})\bar{v}_y + \bar{p}S_y \\ (\bar{\rho}\vec{v} \cdot \bar{S})\bar{v}_z + \bar{p}S_z \\ (B \cdot \bar{S})\bar{E} \end{bmatrix} + Det_c, \quad (5)$$

$$\bar{F}_V \bar{S} = \begin{bmatrix} 0 \\ \bar{D}_x \cdot \bar{S} \\ \bar{D}_y \cdot \bar{S} \\ \bar{D}_z \cdot \bar{S} \\ (B \cdot \bar{S}) + \bar{q} \end{bmatrix} + \begin{bmatrix} 0 \\ 0 \\ 0 \\ 0 \\ Det_v \end{bmatrix},$$

$$B = \begin{bmatrix} \bar{D}_x \cdot \bar{v}' \\ \bar{D}_y \cdot \bar{v}' \\ \bar{D}_z \cdot \bar{v}' \end{bmatrix}, \quad (6)$$

$$Det_c = \begin{pmatrix} 0 \\ v'_x((\rho\vec{v})' \cdot \bar{S}) \\ v'_y((\rho\vec{v})' \cdot \bar{S}) \\ v'_z((\rho\vec{v})' \cdot \bar{S}) \\ H'((\rho\vec{v})' \cdot \bar{S}) \end{pmatrix}, \quad Det_v = \begin{pmatrix} \bar{D}'_x \cdot \bar{v}' \\ \bar{D}'_y \cdot \bar{v}' \\ \bar{D}'_z \cdot \bar{v}' \end{pmatrix} \cdot \bar{S}, \quad (7)$$

where $D_x = (\tau_{xx}, \tau_{xy}, \tau_{xz})$, $D_y = (\tau_{yx}, \tau_{yy}, \tau_{yz})$, $D_z = (\tau_{zx}, \tau_{zy}, \tau_{zz})$ denote the strain terms, and Det_c and Det_v are the contributions of the deterministic stress terms.

To compute the deterministic stress terms and close the flow control equations, the transport equation for each complex amplitude of unsteady perturbation is obtained by retaining the first-order terms in the basic unsteady flow equation. By casting the first-order linearized equation into the frequency domain, this harmonic perturbation equation—like the time-averaged flow equation—is only spatially relevant. Consequently, only one blade passage is required for each blade row in the unsteady simulation. The flow control equations can be written as

$$\Omega_t \frac{d\tilde{U}}{dt_i} = -\sum_{cellfaces} \tilde{F}_C \tilde{S} + \sum_{cellfaces} \tilde{F}_V \tilde{S} + \Omega_t \tilde{S}_{Ti}, \quad (8)$$

$$\tilde{F}_C \tilde{S} = \begin{pmatrix} \tilde{\rho} \tilde{v} \cdot \tilde{S} \\ \tilde{v}_x (\tilde{\rho} \tilde{v} \cdot \tilde{S}) + \tilde{v}_x (\tilde{\rho} \tilde{v} \cdot \tilde{S}) + \tilde{p} \tilde{S}_x \\ \tilde{v}_y (\tilde{\rho} \tilde{v} \cdot \tilde{S}) + \tilde{v}_y (\tilde{\rho} \tilde{v} \cdot \tilde{S}) + \tilde{p} \tilde{S}_y \\ \tilde{v}_z (\tilde{\rho} \tilde{v} \cdot \tilde{S}) + \tilde{v}_z (\tilde{\rho} \tilde{v} \cdot \tilde{S}) + \tilde{p} \tilde{S}_z \\ \tilde{H} (\tilde{\rho} \tilde{v} \cdot \tilde{S}) + \tilde{H} (\tilde{\rho} \tilde{v} \cdot \tilde{S}) \end{pmatrix}, \quad \tilde{F}_V \tilde{S} = \begin{pmatrix} 0 \\ \tilde{D}_x \cdot \tilde{S} \\ \tilde{D}_y \cdot \tilde{S} \\ \tilde{D}_z \cdot \tilde{S} \\ \tilde{B} \cdot \tilde{S} + \tilde{q} \end{pmatrix}, \quad (9)$$

$$\tilde{B} = \begin{pmatrix} \tilde{D}_x \cdot \tilde{v} + \tilde{D}_x \cdot \tilde{v} \\ \tilde{D}_y \cdot \tilde{v} + \tilde{D}_y \cdot \tilde{v} \\ \tilde{D}_z \cdot \tilde{v} + \tilde{D}_z \cdot \tilde{v} \end{pmatrix} \quad (10)$$

and the harmonic source term is calculated as

$$\tilde{S}_{Tk} = -I\omega_k \tilde{U}. \quad (11)$$

The laminar viscosity is calculated from the mean flow variables. The turbulence can be calculated from the eddy viscosity model, where the eddy viscosity is assumed to be unaffected by unsteady disturbances, so the total viscosity term can be written in a linear form as

$$\begin{aligned} \tilde{\tau}_{ij} &= (\mu + \mu_t) \left(\frac{\partial \tilde{v}_i}{\partial x_j} + \frac{\partial \tilde{v}_j}{\partial x_i} - \frac{2}{3} (\nabla \cdot \tilde{v}) \delta_{ij} \right), \\ \tilde{\tau}_{ij} &= (\mu + \mu_t) \left(\frac{\partial \tilde{v}_i}{\partial x_j} + \frac{\partial \tilde{v}_j}{\partial x_i} - \frac{2}{3} (\nabla \cdot \tilde{v}) \delta_{ij} \right), \end{aligned} \quad (12)$$

$$\tilde{q} = -(\kappa + \kappa_t) \nabla T \cdot \tilde{S},$$

$$\tilde{q} = -(\kappa + \kappa_t) \nabla T \cdot \tilde{S}.$$

The deterministic stress terms are determined directly by the harmonic values, thus closing the flow control equation. The stress resulting from two fluctuations f' and g' is calculated as

$$\overline{f'g'} = 2 \left(\tilde{f}_R \tilde{g}_R + \tilde{f}_I \tilde{g}_I \right). \quad (13)$$

As described above, the NLH method decomposes the periodic unsteady flow into the sum of the time-averaged flow and its periodic disturbance, the latter being solved for directly in the frequency domain, that is, without resolving the transient. Also, only one blade passage for each blade row needs to be modeled in the NLH method. Consequently, the computational cost of the periodic unsteady flow

using the NLH method can be reduced significantly. The simulation efficiency and accuracy of the NLH method have been studied and validated extensively for various turbomachinery applications.^{32–37}

B. Studied rotor and DTI design

The investigated geometrical configuration is shown schematically in Fig. 1. The well-known transonic NASA Rotor 37—which has been studied experimentally at the NASA Lewis Research Center³⁸—serves as the base compressor for the present study, and its primary design parameters are described in Table I. Because of its large inlet tip relative Mach number, Rotor 37 features strong tip leakage flow (TLF)–passage-shock interaction under near-stall conditions,³⁹ so it is a typical tip-critical rotor and is especially suitable for the present tip-injection study.

As shown in Fig. 1, tip injection works by using a shroud-mounted injector to shoot high-energy fluid into the tip flow passage of the compressor, so as to improve endwall flow conditions and, thus, enhance the operating stability of the compressor. Studies have shown that Coandă injectors are more effective than other type injectors (e.g., angled slot injectors) because Coandă injectors can generate a high-speed jet along the shroud endwall at the rotor tip region due to the wall attachment effect (Coandă effect),²⁰ so it was also adopted in the present study. The structural design of the present Coandă injector [Fig. 1(c)] references the prototype design from the NASA Glenn Research Center⁶ [Fig. 1(b)]. The critical downstream flow path of each Coandă injector consists of two eccentric circular arcs O_1 and O_2 . The circular arc O_1 is tangent to the shroud, and the position of the tangent point is determined by the distance a between injector and blade LE. The contraction or expansion of the flow path cross section is controlled by the circular arc O_2 , where the center of circular arc O_2 is adjusted by the eccentric distance de_1 and de_2 , and the radius r_2 is determined based on the injector outlet height h and the center position of circular arc O_2 . Twelve discrete injectors are arranged uniformly in the circumferential direction of the shroud [Fig. 1(a)], and the circumferential width of each injector is given by the parameter θ .

C. Numerical validation

1. Grid generation strategy

In order to apply the NLH method to the numerical simulation of DTI device, the whole computational model is divided into three parts, namely, the stationary inlet domain, the rotor domain, and the flow channel of the tip injector, as shown in Fig. 2. The stationary inlet domain extends from the upstream inlet boundary to ca. 5% of the axial chord length (C_{ax}) upstream of the blade LE, and a rotor–stator interface is set between the stationary inlet domain and the rotor domain. Much effort went into generating a high-quality multi-block structured grid using the NUMECA TurboGrid and IGG software packages in cooperation. The grids of the inlet domain and tip injector are generated in IGG with multi-H blocks to satisfy the simulation requirement of high grid orthogonality, as shown in Figs. 2(b) and 2(c). One blade passage is constructed for the inlet domain with a periodicity of 12 such that a periodic full non-matching boundary can be used to connect it directly with the grid of the tip injector, as shown in Fig. 2(a). The grid of a single rotor blade passage is generated in TurboGrid using an O4H type topology, where the blade is surrounded by an O block and the rest is filled with H blocks, as shown

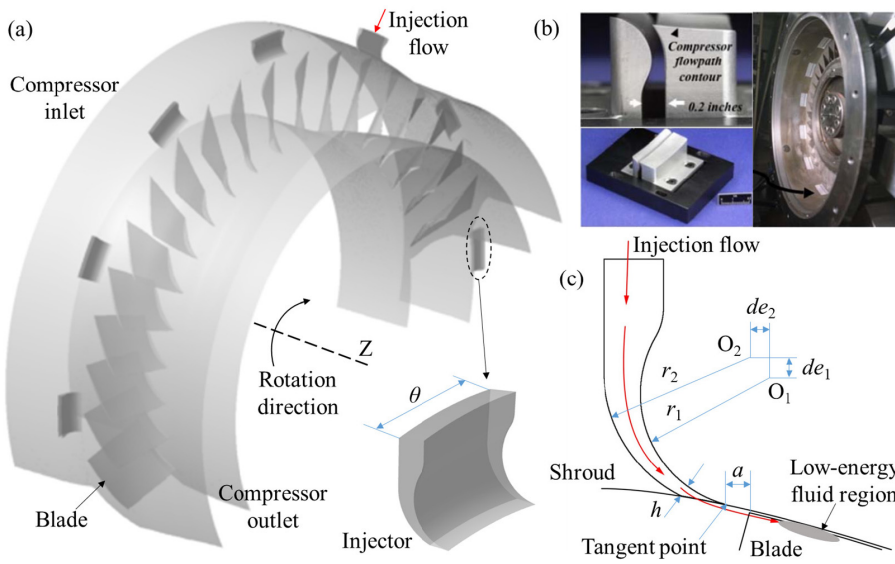


FIG. 1. Rotor 37 and discrete tip injection (DTI) design in present study and Ref. 6.

in Fig. 2(b). To capture accurately the flow in the boundary layer, all grids near solid walls are refined strictly to ensure a y^+ of less than 2. Also, since the NLH method is based on the spatial Fourier decomposition of parameters in the circumferential direction, there are some recommendations on the resolution of the circumferential grid nodes in blade rows. Vilmin *et al.*⁴⁰ suggested that the number of grid nodes in the circumferential direction should be determined according to the number of harmonics (N_H) as well as the number of blades in the upstream blade row (N_u) and the downstream blade row (N_d), as follows:

$$\begin{aligned} Pts_{upstream} &= 30 \cdot N_H \cdot \frac{N_d}{N_u}, \\ Pts_{downstream} &= 30 \cdot N_H \cdot \frac{N_u}{N_d}. \end{aligned} \quad (14)$$

2. Numerical settings

The NLH method-based numerical simulation is implemented in the NUMECA FINE/Turbo code, with the one-equation eddy-viscosity Spalart–Allmaras model used for turbulence modeling. The spatial and temporal terms are discretized using the second-order central

scheme and the four-stage explicit Runge–Kutta scheme, respectively. As shown in Fig. 2, the boundary conditions are set as follows:

- (1) The radial distributions of total pressure Pt_1 and total temperature Tt_1 are implemented at the compressor inlet boundary;
- (2) The injectors are supplied with air at a constant total pressure Pt_2 of 170 000 Pa and a constant total temperature Tt_2 of 288.15 K;
- (3) The operating condition of the compressor is adjusted by varying the average static pressure Ps_2 at the compressor outlet

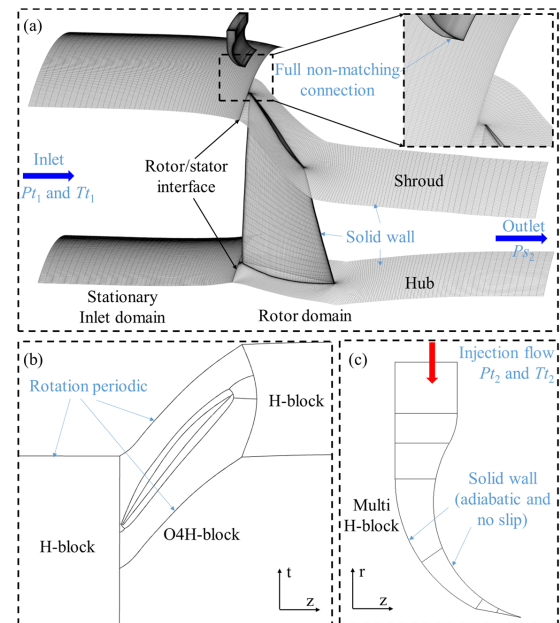


FIG. 2. Computational grids of Rotor 37 with DTI.

TABLE I. Main design parameters of Rotor 37.

Parameter	Value
Number of blades	36
Shaft speed (rpm)	17 188.7
Blade tip clearance (mm)	0.356
Inlet tip relative Mach number	1.48
Tip solidity	1.288
Inlet hub/tip ratio	0.70
Aspect ratio	1.19

07 August 2023 15:29:00

boundary, and an accuracy of 100 Pa is used under near-stall conditions;

- (4) On the lateral side of the computational domain for each row, the same periodic boundary treatment as in the steady simulation is utilized for the time-averaged equations, while the inter-blade phase-angle approach^{30,41} is applied for the harmonics;
- (5) All solid wall surfaces are set to be adiabatic and no-slip conditions, including hub and shroud endwalls, blade surface, and the wall of injector;
- (6) For the rotor–stator interface, the 1D nonreflecting boundary condition is used for the harmonics, and the flow variables on each side of the interface are calculated based on the reconstructed time-averaged values and harmonics. The continuity of flow variables across the interface and the accuracy of the simulation results both increase with the number of harmonics given during the simulation. Lange *et al.*³⁶ proved that five or more harmonics are usually required to analyze accurately the blade interaction near the blade LE. Therefore, six harmonics are adopted for each blade passage in the simulation of Rotor 37 with and without optimal DTI, and three harmonics are adopted during the optimization process to increase the optimization efficiency.

3. Validation of numerical results

The numerical validations of Rotor 37 without DTI are shown in Figs. 3 and 4. For the inlet and rotor domains, the simulation results using two refined grids are compared in Fig. 3: a grid of 2.5×10^6 nodes is used for the optimization study, and a grid of 5.3×10^6 nodes (101 layers in the radial direction, including 25 layers in the tip clearance) is used to guarantee grid independence. The comparison of the simulation results for the two refined grids shows that there is almost no difference in the predicted performance maps and near-stall operating points, which indicates that the grid of 2.5×10^6 nodes is sufficient for the present optimization study.

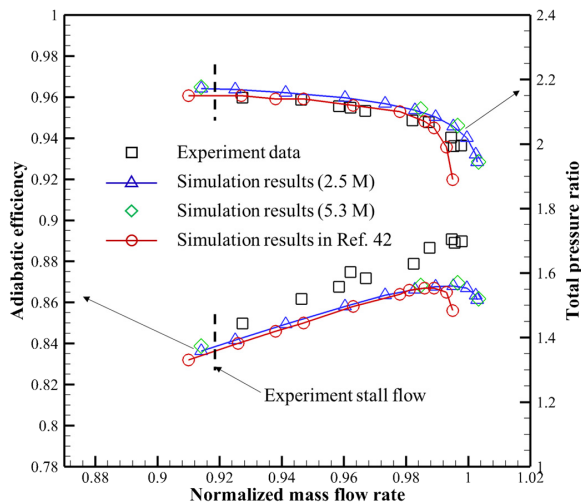


FIG. 3. Validation of numerical results for Rotor 37, including grid independence and performance comparison with experimental³⁸ and other computational fluid dynamics results.⁴²

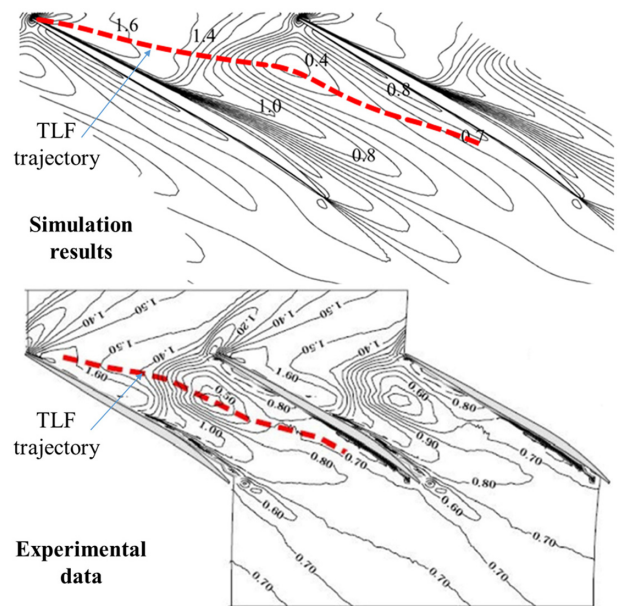


FIG. 4. Comparison of relative Mach number contours at 95% span under near-stall condition.³⁸

As shown in Fig. 3, the predicted total pressure ratio in the present study and Ref. 42 agrees well with the experimental data, while the adiabatic efficiency in both studies is slightly underestimated. This is consistent with almost all other RANS-based simulation results for NASA Rotor 37 in the published literatures.^{16,43,44} The reasons behind the underestimation of the adiabatic efficiency are still not particularly clear,⁴³ but there are several possible reasons. Cui *et al.*⁴⁴ suggested that the main reason is that the flow in transonic Rotor 37 is too complex (especially in the blade tip region), with passage shock, boundary layer separation, TLF, vortex, and extremely complex interactions between them. It is, therefore, very challenging for RANS-based methods to accurately predict these complex flows. In addition, some neglected model details in the CFD simulation (e.g., hub fillet and hub leakage flow) and the accuracy of the boundary conditions can also have an impact on the prediction results.^{42,45} For example, the adiabatic wall assumption is the standard boundary condition used to simulate endwalls and blade of compression systems; however, the simulation results of Bruna and Turner⁴² show that the underestimation of the adiabatic efficiency of Rotor 37 can be partially improved by using isothermal boundary condition on the shroud endwall.

A comparison of the simulation results in this study with Ref. 42 also indicates that the peak efficiency and near-stall operating points predicted in this study are all closer to the experimental values. Figure 4 compares the relative Mach number contours at 95% span and TLF trajectory under near-stall condition. The structure of the detached passage shock and the TLF trajectory shown in the experiment are predicted well, as is the low-velocity region caused by the TLF–passage-shock interaction, which is the primary reason for shroud endwall blockage (SEB) formation.⁴⁶ With the above performance and flow field validation, the adopted numerical method is competent for the present optimization work.

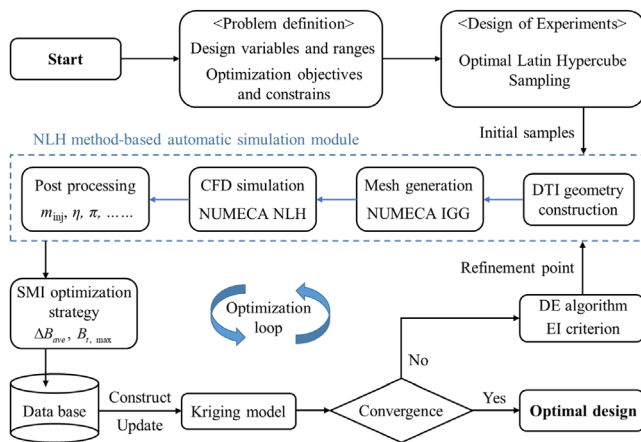


FIG. 5. DTI design optimization framework.

III. DTI DESIGN OPTIMIZATION FRAMEWORK

A. Overall architecture

The established DTI design optimization framework is shown in Fig. 5. An adaptive kriging-based optimization technique is adopted to efficiently search for the optimal solution in the design space, which is combined with a NLH method-based simulation module and a blockage attenuation-based SMI optimization strategy to automatically implement DTI designs. The optimization process can be divided into two steps, as follows:

The first step is the design of experiment (DOE), in which a certain number of initial sample points are arranged uniformly in the design space by the optimal Latin hypercube sampling method,⁴⁷ conducting a preliminary exploration of the design space and a rough kriging approximation of the original optimization problem.

The second step is the iterative updating of the kriging model and optimal solution, in which the refinement points considering both exploration and exploitation are selected iteratively by the differential evolution (DE) algorithm⁴⁸ and kriging-based expected improvement (EI) criterion,⁴⁹ achieving an efficient and full search of the design space. With the assistance of the adaptive kriging model, the selection of sample points is no longer blind but arranged according to the characteristics of the optimization problem, which can greatly reduce the demand for the overall sample points and significantly improve the optimization efficiency. The convergence of the optimization iterations is determined by monitoring the trend of the objective function.

Whenever a new DTI design is selected, the NLH method-based simulation module can be invoked automatically for geometry construction, meshing, numerical simulation, post-processing, and so on. Then, the blockage attenuation-based SMI optimization strategy module is activated to perform the calculation of the index and constraint regarding operating stability based on the flow field simulation information. Those designs that cannot converge in the numerical simulation or do not satisfy the constraints are treated by the penalty-function method in the optimization process.

B. Blockage attenuation-based SMI optimization strategy

Numerous flow-mechanism studies have shown that the magnitude of SEB is closely related to the stable operating range of tip-critical rotors. Early experimental studies by McDougall *et al.*⁵⁰ and Suder⁴⁶ showed clearly that the endwall blockage is the crucial property in determining the stall point. Yamada *et al.*^{39,51} investigated numerically the unsteady behavior of the tip leakage vortex (TLV) in a transonic AFC rotor and discovered that the breakdown of the TLV caused a large blockage and flow unsteadiness in the rotor tip passage under near-stall conditions. Recently, Brandstetter *et al.*⁵² observed experimentally that the large blockage due to the breakdown of the TLV caused the flow to spill forward to the leading edge of the adjacent blade under near-stall conditions. This is consistent with one of the two basic stall mechanisms (blade tip stall and tip blockage stall, as shown in Fig. 6) of transonic AFCs (tip-critical rotors) as concluded by Wilke *et al.*⁵³ As also demonstrated by the two basic stall mechanisms,⁵³ the blockage caused by the boundary-layer separation or the TLV is the crucial property for stall inception.

In addition, many studies of tip-injection flow mechanisms have also shown that the reduction of SEB is the main reason for the SMI of tip-critical rotors.^{16,54–57} For instance, Beheshti *et al.*⁵⁴ showed that the large blockage region caused by TLV–shock interaction can result in flow instability and performance drop for the compressor, which can be controlled efficiently by the tip injection by re-energizing the low-energy flow near the tip region. Wang *et al.*¹⁶ studied in detail the blockage reduction, mass-averaged axial velocity increase, and unloading effect caused by tip injection in a transonic rotor, and they found the SMI to be closely related to the blockage reduction within the injection domain.

All of these studies indicate that the SMI caused by DTI can be linked to the blockage attenuation in the rotor tip region, which provides a physics-based index for the SMI optimization of DTI design.

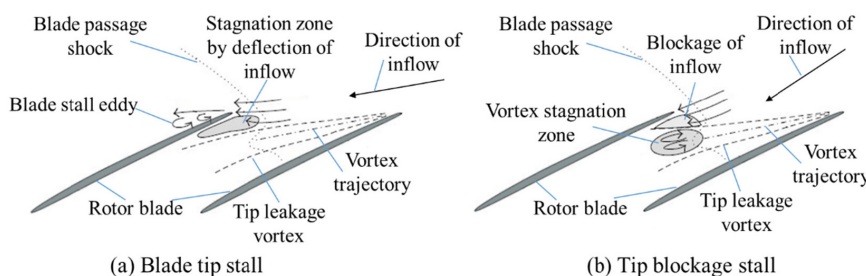


FIG. 6. Basic stall mechanisms of transonic axial flow compressor (AFC).⁵³

07 August 2023 15:29:00

1. Blockage quantification method

A relatively accurate method for quantifying blockage in AFCs is that based on classical boundary-layer theory, as explained by Suder.⁴⁶ However, because of the very complex 3D flow characteristics in the rotor tip region caused by the periodic injection flow, it is not convenient to use classical boundary-layer theory to quantify the SEB in the present study. Therefore, a simplified method proposed by Hoeger *et al.*⁵⁸ is adopted instead, where a local displacement thickness δ_e from the axially reversed flow is used to quantify the SEB. This local displacement thickness considers the blockage of the reversed flow field caused by the TLF and separated boundary layer.

As shown in Fig. 7, the blue dotted line indicates where ρW_z is zero, and the area surrounded by the blue dotted line and the endwall is the axially reversed flow region. At any position Z , the local displacement thickness δ_e indicates that the integral value of ρW_z from the endwall to here equals zero, which is calculated as

$$\int_0^{\delta_e} \rho W_z d\delta = 0. \tag{15}$$

Equation (15) is used to quantify the circumferentially averaged SEB of one blade passage at different axial locations and different time steps. A blockage factor B can be defined as the ratio of the blockage area to the through-flow area and is expressed as

$$B = \frac{\pi(R_s^2 - (R_s - \delta_e)^2)}{\pi(R_s^2 - R_h^2)}, \tag{16}$$

where R_s and R_h are the radii of the shroud and hub endwalls, respectively.

Figure 8 shows the distribution of SEB in Rotor 37 from the leading edge to the trailing edge under four different operating conditions, i.e., choke condition (choked), peak-efficiency condition (PE), design condition (DE), and near-stall condition (NS). As the compressor throttles progressively from the choke condition to the near-stall condition, the axial location of the maximum SEB moves gradually toward the blade LE and the maximum SEB increases gradually. This is a good reflection of the forward shift of the passage shock and the enhanced intensity of the TLV during the throttling process, as shown in Fig. 9 and revealed in previous studies of Rotor 37.^{39,59} Also, the comparison of the SEB in the rear part of the blade passage clearly reflects the aggravation of the separation of the suction-surface boundary layer at the near-stall condition compared with that at the design

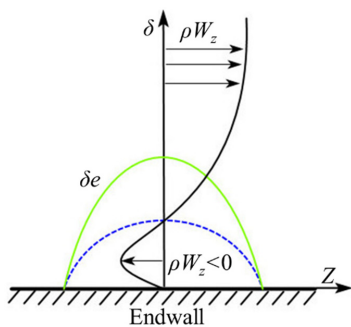


FIG. 7. Displacement thickness caused by axially reversed flow.

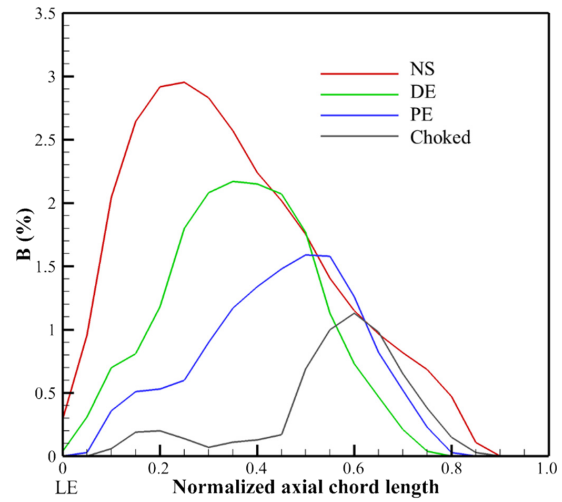


FIG. 8. Distribution of shroud end wall blockage (SEB) of Rotor 37 under different operating conditions.

condition. Therefore, the defined blockage factor is qualified for quantifying the SEB and is competent for the current design optimization study.

2. DTI effects and unsteady blockage correlation

As shown in Fig. 1, Rotor 37 with an initial Coandă injector design is used as an example to research the unsteady development of the SEB and the underlying flow mechanisms. A parameter ΔB is defined as the blockage difference between Rotor 37 with and without tip injection and is used to visualize intuitively the effect of DTI. Figure 10 shows the unsteady variation of ΔB from the leading edge to the trailing edge in blade passage ① (shown in Fig. 11) during its passage through a tip injector under near-stall condition, where the abscissa represents the dimensionless time t calculated from the blade rotation time of one pitch. Figure 11 compares the instantaneous distributions of TLF, axially reversed flow region at 98.5% span, and injector outlet velocity of Rotor 37 with and without the initial injector.

As shown in Fig. 10, within the region where the DTI is effective, the SEB at close to 20% of C_{ax} —which is the position of the maximum

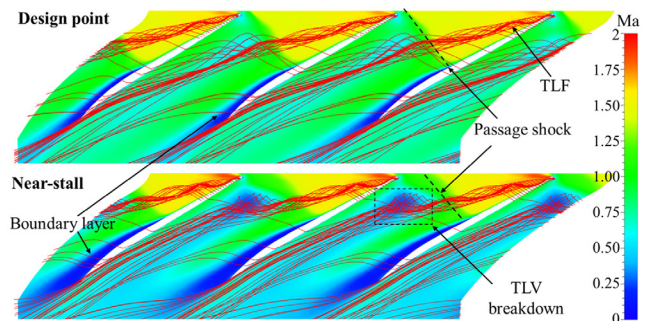


FIG. 9. Relative Mach number contour at 95% span and tip leakage flow (TLF) pattern of Rotor 37 at different operating points.

07 August 2023 15:29:00

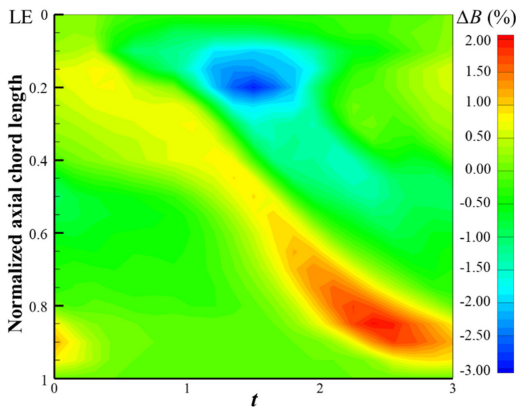


FIG. 10. Unsteady variation of SEB for Rotor 37 with initial DTI.

SEB under near-stall condition as shown in Fig. 8—is decreased significantly. This indicates that the tip injection is effective at reducing the endwall blockage caused by the TLF–passage-shock interaction. This is also evident from the flow field in blade passage ③ shown in Fig. 11, where the intensity of the TLV and the area of the corresponding axially reversed flow region are weakened significantly when the jet flow is injected into the blade tip passage. However, outside the effective region of the DTI, there is a slight enhancement in SEB between 10%–45% of C_{ax} , as reflected by the flow features in blade passage ②. In addition, tip injection aggravates the boundary-layer separation of the suction surface near the blade trailing edge, especially when the blade is located in the middle of two adjacent tip injectors, as shown in blade passage ④.

3. Operating stability optimization strategy

The analysis of the unsteady SEB development reveals that the DTI affects the blade tip flow field in two opposite ways. The positive aspect is the significant reduction in SEB associated with the TLV, which is the main reason for the improvement of the compressor operating stability by the DTI device. The negative aspect is the increased separation of the suction-surface boundary layer near the blade trailing edge, which is not conducive to improving the compressor operating stability. Therefore, there is a logical guideline for the optimal DTI design considering the SMI objective, that is, maximizing

the SEB attenuation gain in the front part of the blade tip passage, while, at the same time, controlling well the suction-surface boundary-layer separation near the blade trailing edge within the tip region.

Inspired by this, an objective function ΔB_{ave} and a constraint B_t are constructed under near-stall condition to guide the SMI optimization of the DTI design. The objective ΔB_{ave} is defined as the spatiotemporal average of all negative ΔB between 0% and 50% of C_{ax} in an injection period ($0 \leq t \leq 3$), which is calculated as

$$\Delta B_{ave} = \frac{\int_0^3 \int_0^{0.5} \Delta B dy dt}{\int_0^3 \int_0^{0.5} 1 dy dt}, \quad \text{region of } \Delta B \leq 0 \quad (17)$$

and is used to characterize the endwall blockage attenuation efficiency caused by the tip injection. The constraint $B_{t,max}$ is defined as the maximum SEB near the blade trailing edge (from 60% to 100% of C_{ax}) during an injection period, which can be expressed as

$$B_{t,max} = \max(B), \quad \text{within 60% to 100% } C_{ax}. \quad (18)$$

$B_{t,max}$ is limited during the design optimization process to control the negative effect of the new DTI design.

C. Optimization problem construction

Defining the optimization problem involves selecting the design variables and their ranges and constructing the optimization objectives and constraints. As shown in Fig. 1, six independent geometric control parameters of the present DTI design are selected as the design variables, that is, $a, h, r_1, de_1, de_2,$ and θ , and their ranges are listed in Table II.

The optimal DTI design should consider improving not only the stable operating range but also some other important objectives. In the present study, improving the stable operating range and reducing the injection mass flow rate are pursued simultaneously, so it is necessary to minimize simultaneously the negative ΔB_{ave} and the injection mass flow rate m_{inj} under near-stall condition. Therefore, a comprehensive objective function constituted by the normalized ΔB_{ave} and m_{inj} is used to drive the DTI design optimization. Also, $B_{t,max}$ is used as an optimization constraint to control the growth of the suction boundary layer near the blade trailing edge and its negative impact on the operating stability of the compressor. Consequently, the optimization problem can be summarized as

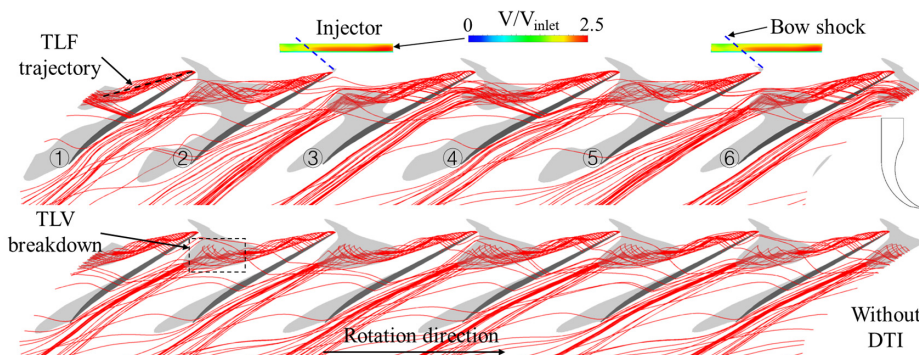


FIG. 11. Instantaneous distributions of TLF and reversed flow region of Rotor 37 with and without initial DTI design.

TABLE II. Ranges of design variables.

Design variable	Lower bound	Upper bound
a	-30% of C_{ax}	-5% of C_{ax}
r_1 (cm)	0.5	2
de_1 (cm)	0.0	0.5
de_2 (cm)	-0.25	0.25
θ (deg)	3.0	20
h	τ	4τ

$$\begin{aligned}
 obj(X) &= \min(C_1 \Delta B'_{ave} + C_2 m'_{inj}) \\
 \text{subject to: } & DV_i^l \leq DV_i \leq DV_i^u \\
 & B_{t,max} \leq 1.5\%,
 \end{aligned}
 \tag{19}$$

where X is the vector of the design variables, C_1 and C_2 are the weight coefficients ($C_1 = C_2 = 0.5$), and $\Delta B'_{ave}$ and m'_{inj} are the normalized objective parameters calculated as following form:

$$\begin{aligned}
 \Delta B'_{ave} &= \frac{\Delta B_{ave} - \min(\Delta B_{ave})}{\max(\Delta B_{ave}) - \min(\Delta B_{ave})}, \\
 m'_{inj} &= \frac{m_{inj} - \min(m_{inj})}{\max(m_{inj}) - \min(m_{inj})}.
 \end{aligned}
 \tag{20}$$

During the design optimization process, the minimum and maximum values of each objective parameter are determined from the existing samples.

IV. OPTIMIZATION RESULTS AND DISCUSSION

A. Optimal DTI design

The design optimization is accomplished on a workstation with a 48-core processor and 192 GB RAM. A sufficiently large number of 102 initial sample points (17 times the number of the design variables) is used to implement sufficient initial exploration of the design space. The parallel calculation of initial sample points makes full use of computing resources and, thus, reduces the number of subsequent refinement points calculated one by one and the total optimization time. During the optimization loop, 65 refinement points are selected by the kriging-based EI criterion and added to the database to update the optimal solution.

Table III presents the values of the design variables and objective parameters for the optimal DTI design, and its geometrical shape and installation location are shown in Fig. 12. The effectiveness of the optimal DTI design is shown in Fig. 13 by comparing the performance maps of Rotor 37 with and without the optimal DTI design. Since the air supply of the DTI is from an external air source, the calculation of the compressor aerodynamic performance must account for the energy balance by removing the energy from the external source to allow a better comparison with the original compressor.^{16,60}

TABLE III. Design variables and objective parameters of optimal DTI design.

Parameter	a	r_1	de_1	de_2	θ	h	ΔB_{ave}	m_{inj}/m_{NS}
Value	-11.94%	0.98	0.12	0.07	17.24	1.12	-1.74%	0.72%

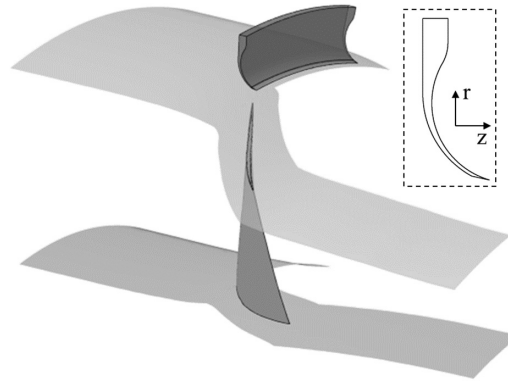


FIG. 12. Geometrical shape and installation location of optimal DTI design.

Therefore, the total pressure ratio and adiabatic efficiency are calculated as

$$\pi^* = [m_2 P t_2 - m_0 (P t_0 - P t_1)] / m_2 P t_1, \tag{21}$$

$$\eta = \frac{(\pi^{*(k-1)/k} - 1)}{[m_2 T t_2 - m_0 (T t_0 - T t_1)] / (m_1 T t_1 + m_0 T t_0) - 1}, \tag{22}$$

where the subscripts 0, 1, and 2 indicate the outlet of the injector, the inlet of the compressor, and the outlet of the compressor, respectively.

As shown in Fig. 13, the stable operating range of Rotor 37 is extended significantly by using the optimal DTI design, with a significant reduction in the minimum mass flow rate and a slight increase in the maximum mass flow rate. Also, the aerodynamic performance of the compressor—especially the total pressure ratio—is improved slightly over the entire operating range. The exact quantifications of the improvement in aerodynamic performance under the three operating conditions (PE, DE, and NS) and the extension of stable

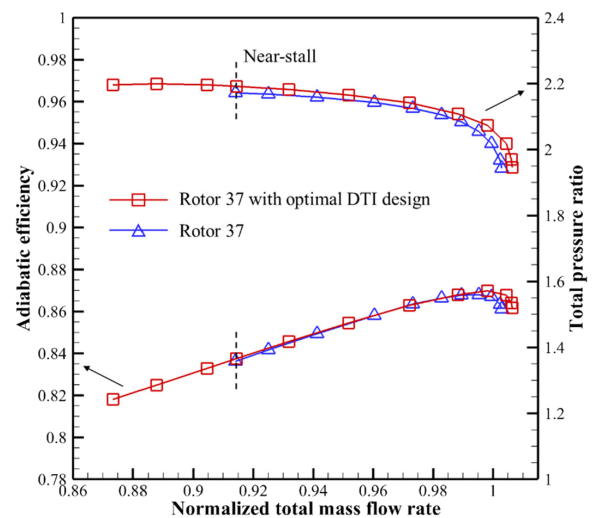


FIG. 13. Comparison of performance maps of Rotor 37 with and without optimal DTI design.

TABLE IV. Performance and stability improvement of Rotor 37 with optimal DTI design.

Improvement	PE	DE	NS
$\Delta\pi$	0.88%	0.61%	0.92%
$\Delta\eta$	0.18%	0.06%	0.12%
$\Delta\varphi_{stall}$		4.46%	

operating stability at low mass flow rate conditions are shown in Table IV. The operating stability improvement is calculated as the relative change of the stalling flow coefficient, that is,

$$\Delta\varphi_{stall} = ((\varphi_{stall})_{SW} - \varphi_{stall})/(\varphi_{stall})_{SW}, \quad (23)$$

where $(\varphi_{stall})_{SW}$ denotes the stalling flow coefficient of Rotor 37 with no tip injection. The optimal DTI design significantly reduces the stalling flow coefficient of Rotor 37 by 4.46% and increases the total pressure ratio by about 0.8% without causing any reduction in the adiabatic efficiency of the compressor, indicating its advantage over the DTI designs in the literature.^{14,21}

Comparing the extension of the stable operating range caused by the present optimal DTI design with that of similar DTI designs available in the literature offers a more intuitive visualization of the effectiveness of the present DTI design optimization method. Strazisar *et al.*²⁰ measured experimentally the operating stability improvement of NASA Stage 35 at different injection mass flow rates, where the type, number, and installation of the injectors were generally consistent with those in the present study, that is, 12 Coandă injectors installed uniformly in the circumferential direction. Since the aerodynamic stability of Stage 35 is dominated by Rotor 35, and since Rotors 37 and 35 can be expected to exhibit similar results^{55,61} because they have similar aerodynamic designs (e.g., the same flow path and equal blade tip speed, blade chord, and aspect ratio), the results of Stage 35 are considered appropriate to show the advantages of the present optimal DTI design. Figure 14 compares the operating stability improvement in the present study and Ref. 20. As shown, under the premise of achieving the same improvement in operating stability, the required injection mass flow rate with the present optimal DTI design is significantly smaller than that with other DTI designs in Ref. 20, that is, ca.

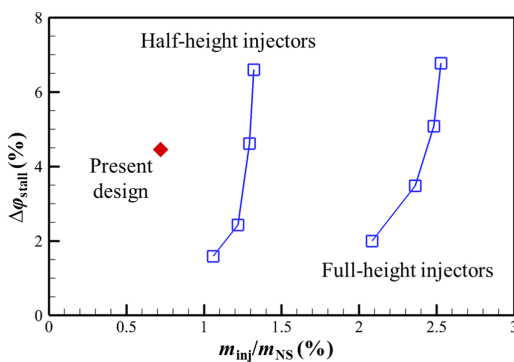


FIG. 14. Comparison of stalling flow coefficient reduction for present optimal DTI design and DTI designs in Ref. 20.

55% of the mass flow rate required with the half-height injector and 30% of the mass flow rate required with the full-height injector.

B. Mechanisms of operating stability enhancement

A detailed unsteady analysis of the internal flow field of Rotor 37 with the optimal DTI design was carried out using the NLH method to help understand the periodic unsteadiness of the compressor caused by DTI and the mechanism by which the DTI design enhances the compressor stability.

Figure 15 shows the unsteady variation of ΔB from the leading edge to the trailing edge in blade passage ① (as shown in Fig. 16) under near-stall condition. The optimal DTI design significantly reduces the SEB between 10% and 45% of C_{ax} over a wide range of injection period, and the SEB near the blade trailing edge is effectively limited with a maximum blockage increase of less than 0.5%. Figure 16 compares the instantaneous distributions of the TLF and axially reversed flow region at 98.5% span for Rotor 37 with and without the optimal DTI design. It is clear that when the blade is located in the effective region of the injector (e.g., blade passage ③), the TLF trajectory is blown significantly closer to the suction side of the blade, which brings the direction of the TLF closer to that of the main flow. Also, because of the re-energizing of the injection flow on the TLV, the intensity of the TLF is significantly weakened when after passing through the passage shock. Consequently, the reverse flow region associated with the TLV is controlled effectively, which is one of the main reasons for the reduced SEB in the front part of the blade passage in Fig. 15.

Looking at the flows in blade passages ③, ④, ⑤, and ⑥ in Fig. 16, there is a cycle showing that the TLV expands and migrates forward but is then suppressed and forced downstream by the injection flow. Also, it is interesting to note that the recovery of the TLF trajectory is basically complete when the blade rotates to the position of blade passage ④, while the recovery of the TLF magnitude lags behind that of the TLF trajectory until the position of blade passage ⑤. This is why DTI is effective in extending the operating stability of the compressor without the need for continuous circumferential injection. Wang *et al.*¹⁶ investigated the effect of a DTI device on the tip flow field in an transonic AFC rotor using a time-accurate unsteady simulation method, and they also observed this hysteresis effect.

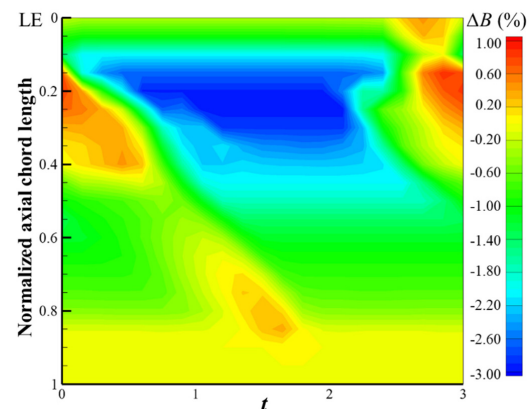


FIG. 15. Unsteady variation of SEB for Rotor 37 with optimal DTI design.

07 August 2023 15:29:00

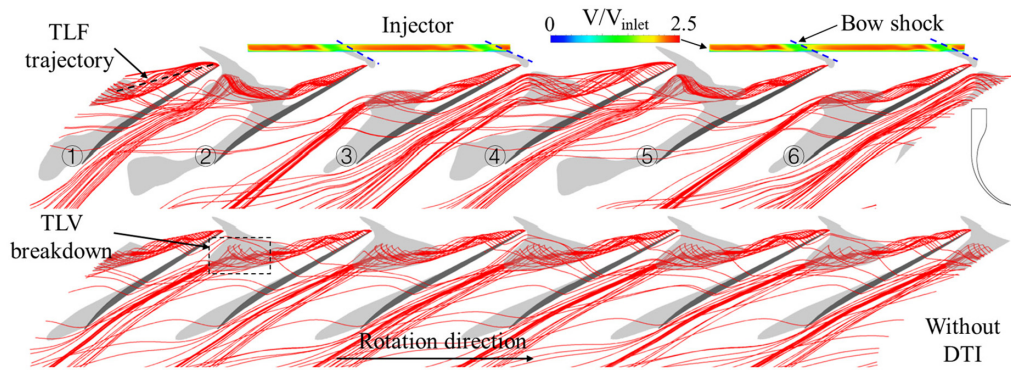


FIG. 16. Instantaneous distributions of TLF and reversed flow region of Rotor 37 with and without optimal DTI design.

Figure 17 shows the axial velocity distribution in the injector and rotor passage at different xz planes. One can observe the gradual acceleration of the fluid in the injector, which is then injected into the rotor tip region. The injection flow leaving the injector outlet is completely attached to the shroud endwall, and the height of the injection flow is approximately the same as that of the TLV core, which not only reduces the impact on the upstream incoming flow but also improves the control of the downstream TLF, thus illustrating the effect of the optimal DTI design. The end of each injection flow (denoting the interaction surface between injection flow and TLF) and the color of the TLV core clearly demonstrate the progressive control of the injection flow on the TLF trajectory and the TLV magnitude as the blade moves from partial to full entry into the effective region of the injector. The injection flow obviously pushes the TLV downstream of the blade passage and significantly reduces the intensity of the TLV.

Figure 18 shows instantaneous distributions of blade profile pressure at 98.5% span and TLF mass flow rate for Rotor 37 with the optimal DTI design. The TLF mass flow rate is calculated as the mass flow across the plane formed by the camber line of the blade tip profile and the radial direction in tip clearance. It can be found that the TLF mass

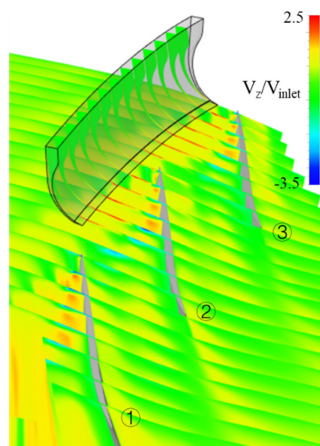


FIG. 17. Axial velocity distribution showing injection-flow-TLV interaction.

flow rate is correlated positively with static pressure difference between blade pressure and suction surfaces. When the blade LE is located in the effective region of the optimal injector (e.g., $t = 0.25$ and $0.5 T$), the suction-surface pressure near the blade LE (0%–5% of C_{ax}) increases and the pressure difference between the pressure and suction surfaces decreases, thus reducing the TLF mass flow rate in the first 5% of C_{ax} . Figure 16 shows that the core part of the TLV is related mainly to the TLF near the blade LE, which was also shown by Hou *et al.*⁶² and He *et al.*⁶³ Therefore, the reduced mass flow rate of the TLF near the blade LE is also very important for the decreased intensity of the TLV.

How the injection flow improves the flow field in the blade tip region—including controlling the TLF trajectory and TLV intensity—can be seen more intuitively from the variations in the flow angle at blade inlet and the axial momentum at blade outlet, as shown in Figs. 19 and 20. The relative positions of the blade and DTI at each time step are shown with reference to Fig. 18. It is clear that the injection flow significantly reduces the inlet flow angle at the blade tip and increases the axial momentum of the tip flow field, which helps improve the compressor operating stability. The inlet flow angle at the blade tip decreases gradually from the beginning of the blade into the effective region of the injector, reaches its minimum in the middle region of the injector, and then recovers gradually until the next injector. However, the maximum increase of axial momentum at blade outlet occurs when the blade is located in the middle of two adjacent injectors. This is consistent with the pattern in Fig. 16 where the recovery of the TLV magnitude lags behind that of the TLF trajectory.

In summary, the main reason for the improved operating stability of the compressor is deemed to be the significant attenuation and delayed recovery of SEB, which, in turn, is attributed mainly to the efficient DTI flow, including its control of the TLF trajectory and its re-energizing of the low-velocity flow in the blade tip region, as well as its reduction of the TLF mass flow rate near the blade LE.

V. CONCLUSIONS

An efficient DTI design framework for transonic AFCs is established by integrating a NLH method, a blockage attenuation-based SMI design optimization strategy, and an adaptive kriging-based optimization technique. It enables rapid completion of complex DTI designs and facilitates the consideration of collaborative optimization of multiple objectives. The following main conclusions are drawn.

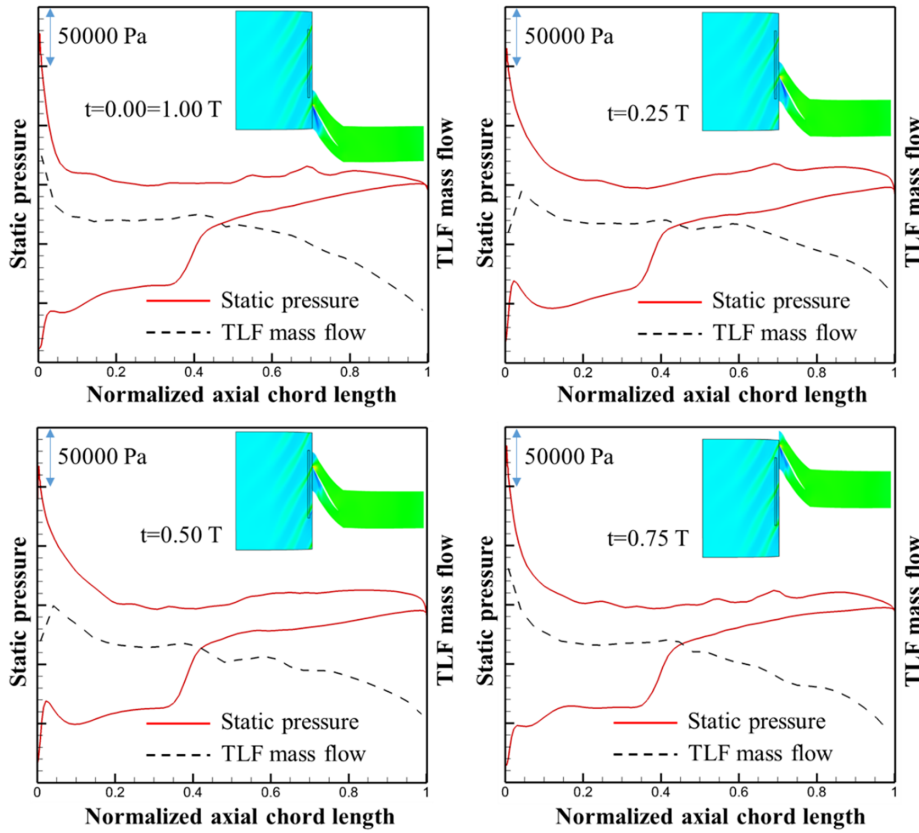


FIG. 18. Instantaneous distributions of profile pressure at 98.5% span and TLF mass flow for Rotor 37 with optimal DTI design.

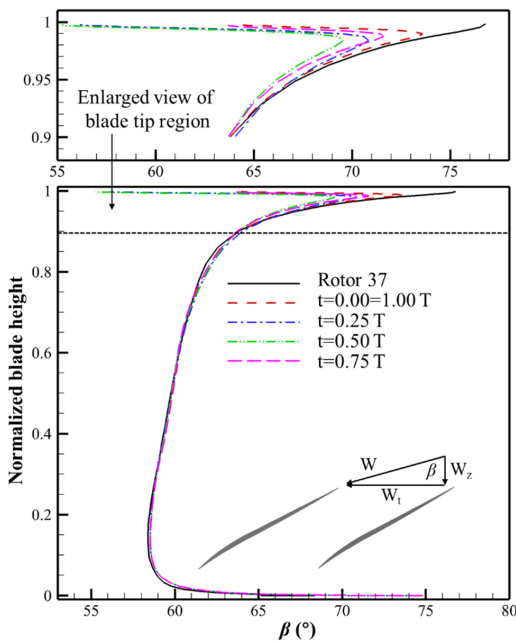


FIG. 19. Instantaneous distributions of flow angle at upstream blade for Rotor 37 with and without optimal DTI design.

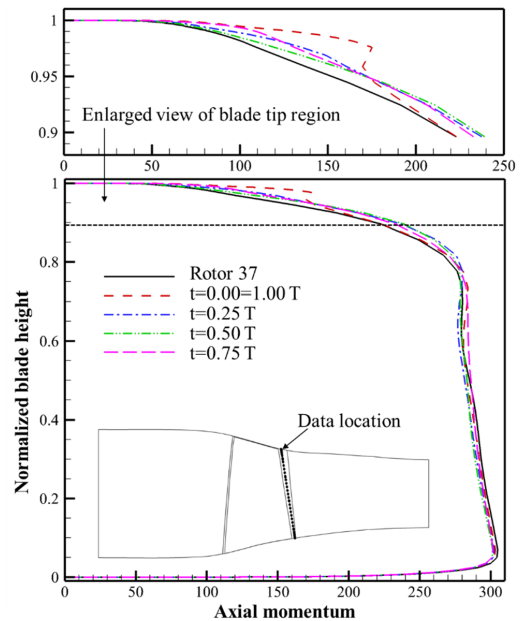


FIG. 20. Instantaneous distributions of axial momentum at downstream blade for Rotor 37 with and without optimal DTI design.

- (1) The variation of critical flow characteristics in the compressor tip region under the action of DTI can be well reflected by the variation of SEB quantified by a local displacement thickness corresponding to the reverse flow field. The optimal DTI design considering the SMI objective should significantly increase the average SEB attenuation in the front part of the blade passage and also well control the deterioration of the maximum SEB near the blade trailing edge. This design strategy avoids the time-consuming simulation of the compressor performance map for each new design during the optimization process, which can be combined with other design objectives to facilitate achieving the collaborative optimization of multiple objectives.
- (2) The established design optimization framework is applied to the Coandă injector design for the transonic NASA Rotor 37, in which the maximum SMI and the minimum injection mass flow rate are pursued simultaneously. The optimal DTI design significantly reduces the stalling flow coefficient of the compressor by 4.46% at a small injection mass flow rate (0.72% of the compressor stalling mass flow), with a slight increase in the aerodynamic performance of the compressor.
- (3) The detailed unsteady flow field analysis based on the NLH method demonstrates that the main reason for the improved operating stability of the compressor is the significant attenuation and delayed recovery of the SEB in the front part of the blade passage, which, in turn, is attributed mainly to the efficient DTI flow, including its control of the TLF trajectory and its re-energizing of the low-velocity flow in the blade tip region, as well as its reduction of the TLF mass flow rate near the blade LE. Furthermore, this critical flow information further demonstrates the accuracy and applicability of the NLH method for rapid design and flow-mechanism analysis of DTI devices.

ACKNOWLEDGMENTS

The authors gratefully acknowledge the National Science and Technology Major Project (No. 2017-II-0007-0021), the Chinese Postdoctoral Science Foundation (No. 2016M602817), and the China Scholarship Council (No. 202006280244) for their financial support.

AUTHOR DECLARATIONS

Conflict of Interest

The authors have no conflicts to disclose.

Author Contributions

Xuesong Wang: Conceptualization (equal); Funding acquisition (equal); Investigation (equal); Methodology (equal); Software (equal); Writing – original draft (equal). **Jinju Sun:** Funding acquisition (equal); Supervision (equal); Writing – review & editing (equal). **Ernesto Benini:** Supervision (equal); Writing – review & editing (equal). **Peng Song:** Funding acquisition (equal); Project administration (equal); Validation (equal). **Wenzhuo Chen:** Data curation (equal); Software (equal).

DATA AVAILABILITY

The data that support the findings of this study are available from the corresponding author upon reasonable request.

REFERENCES

- ¹F. Gao, W. Ma, G. Zambonini, J. Boudet, X. Ottavy, L. Lu, and L. Shao, "Large-eddy simulation of 3-D corner separation in a linear compressor cascade," *Phys. Fluids* **27**, 085105 (2015).
- ²S. Babu, P. Chatterjee, and A. M. Pradeep, "Transient nature of secondary vortices in an axial compressor stage with a tandem rotor," *Phys. Fluids* **34**, 065125 (2022).
- ³E. Benini and R. Biollo, "Aerodynamics of swept and leaned transonic compressor-rotors," *Appl. Energy* **84**, 1012 (2007).
- ⁴H. Zhu, L. Zhou, T. Meng, and L. Ji, "Corner stall control in linear compressor cascade by blended blade and endwall technique based on large eddy simulation," *Phys. Fluids* **33**, 115124 (2021).
- ⁵T. Meng, X. Li, L. Zhou, H. Zhu, J. Li, and L. Ji, "Large eddy simulation and combined control of corner separation in a compressor cascade," *Phys. Fluids* **34**, 075113 (2022).
- ⁶M. D. Hathaway, "Passive endwall treatments for enhancing stability," NASA Report No. TM-2007-214409, 2007.
- ⁷M. Rolfes, M. Lange, K. Vogeler, and R. Mailach, "Experimental and numerical investigation of a circumferential groove casing treatment in a low-speed axial research compressor at different tip clearances," *J. Turbomach.* **139**(12), 121009 (2017).
- ⁸D. Sun, J. Li, X. Dong, R. Xu, and X. Sun, "Foam-metal casing treatment on an axial flow compressor: Stability improvement and noise reduction," *J. Turbomach.* **144**(1), 011003 (2022).
- ⁹J. Paduano, A. H. Epstein, L. Valavani, J. P. Longley, E. M. Greitzer, and G. R. Guenette, "Active control of rotating stall in a low speed axial compressor," *J. Turbomach.* **115**(1), 48–56 (1993).
- ¹⁰C. M. Van Schalkwyk, J. D. Paduano, E. M. Greitzer, and A. H. Epstein, "Active stabilization of axial compressors with circumferential inlet distortion," *J. Turbomach.* **120**(3), 431–439 (1998).
- ¹¹K. L. Suder, M. D. Hathaway, S. A. Thorp, A. J. Strazisar, and M. B. Bright, "Compressor stability enhancement using discrete tip injection," *J. Turbomach.* **123**(1), 14–23 (2001).
- ¹²X. Liu, J. Teng, J. Yang, X. Sun, D. Sun, C. He, and J. Du, "Calculation of stall margin enhancement with micro-tip injection in an axial compressor," *J. Fluids Eng.* **141**(8), 081109 (2019).
- ¹³W. Wang, W. Chu, H. Zhang, and H. Kuang, "Experimental and numerical study of tip injection in a subsonic axial flow compressor," *Chin. J. Aeronaut.* **30**(3), 907–917 (2017).
- ¹⁴H. Khaleghi, "Effect of discrete endwall recirculation on the stability of a high-speed compressor rotor," *Aerosp. Sci. Technol.* **37**, 130–137 (2014).
- ¹⁵G. Cassina, B. H. Beheshti, A. Kammerer, and R. S. Abhari, "Parametric study of tip injection in an axial flow compressor stage," ASME Paper No. GT2007-27403 (2007).
- ¹⁶W. Wang, B. Liu, J. Lu, J. Feng, W. Chu, and Y. Wu, "Comparative study of tip injection in a transonic and subsonic compressor," *J. Turbomach.* **144**(6), 061009 (2022).
- ¹⁷J. Li, J. Du, C. Nie, and H. Zhang, "Review of tip air injection to improve stall margin in axial compressors," *Prog. Aerosp. Sci.* **106**, 15–31 (2019).
- ¹⁸S. J. Hiller, R. Matzgeller, and W. Horn, "Stability enhancement of a multi stage compressor by air injection," ASME Paper No. GT2009-59868 (2009).
- ¹⁹C. Nie, G. Xu, X. Cheng, and J. Chen, "Micro air injection and its unsteady response in a low-speed axial compressor," *J. Turbomach.* **124**(4), 572–579 (2002).
- ²⁰A. J. Strazisar, S. Thorp, M. M. Bright, K. L. Suder, and D. E. Culley, "Compressor stall control through endwall recirculation," ASME Paper No. GT2004-54295 (2004).
- ²¹S. Weichert, I. Day, and C. Freeman, "Self-regulating casing treatment for axial compressor stability enhancement," ASME Paper No. GT2011-46042 (2011).
- ²²C. T. Dinh, M. W. Heo, and K. Y. Kim, "Aerodynamic performance of transonic axial compressor with a casing groove combined with blade tip injection and ejection," *Aerosp. Sci. Technol.* **46**, 176–187 (2015).

- ²³W. Wang, J. Lu, X. Luo, and W. Chu, "Coupling method of stability enhancement based on casing treatments in an axial compressor," *Aerosp. Sci. Technol.* **95**, 105449 (2019).
- ²⁴H. Okui, T. Verstraete, R. A. Van den Braembussche, and Z. Alsalihi, "Three-dimensional design and optimization of a transonic rotor in axial flow compressors," *J. Turbomach.* **135**(3), 031009 (2013).
- ²⁵P. Song, J. Sun, and K. Wang, "Axial flow compressor blade optimization through flexible shape tuning by means of cooperative co-evolution algorithm and adaptive surrogate model," *Proc. Inst. Mech. Eng., Part A: J. Power Energy* **228**(7), 782–798 (2014).
- ²⁶Q. Du, T. Liu, L. Yang, L. Li, D. Zhang, and Y. Xie, "Airfoil design and surrogate modeling for performance prediction based on deep learning method," *Phys. Fluids* **34**, 015111 (2022).
- ²⁷G. Zhu and B. Yang, "Optimization of slots-groove coupled casing treatment for an axial transonic compressor," *J. Turbomach.* **142**(8), 081003 (2020).
- ²⁸D. Ba, Q. Zhang, J. Du, Z. Li, H. Zhang, and C. Nie, "Design optimization of axial slot casing treatment in a highly-loaded mixed-flow compressor," *Aerosp. Sci. Technol.* **107**, 106262 (2020).
- ²⁹J. H. Kim, K. J. Choi, and K. Y. Kim, "Aerodynamic analysis and optimization of a transonic axial compressor with casing grooves to improve operating stability," *Aerosp. Sci. Technol.* **29**, 81–91 (2013).
- ³⁰L. He and W. Ning, "Efficient approach for analysis of unsteady viscous flows in turbomachines," *AIAA J.* **36**(11), 2005–2012 (1998).
- ³¹T. Chen, P. Vasanthakumar, and L. He, "Analysis of unsteady blade row interaction using nonlinear harmonic approach," *J. Propul. Power* **17**(3), 651–658 (2001).
- ³²E. Guidotti and M. G. Turner, "Analysis of the unsteady flow in an aspirated counter-rotating compressor using the nonlinear harmonic method," ASME Paper No. GT2009-60285 (2009).
- ³³L. Wang, B. Liu, X. Yang, and Z. Cao, "Unsteady simulation of a counter-rotating research compressor using the nonlinear harmonic method," *Proc. Inst. Mech. Eng., Part G: J. Aerosp. Eng.* **227**(3), 415–424 (2013).
- ³⁴B. Liu, B. Zhang, and Y. Liu, "Numerical investigations of impeller-diffuser interactions in a transonic centrifugal compressor stage using nonlinear harmonic method," *Proc. Inst. Mech. Eng., Part A: J. Power Energy* **228**(8), 862–877 (2014).
- ³⁵A. D. Grosvenor, G. S. Rixon, L. M. Sailer, M. A. Matheson, D. P. Gutzwiller, A. Demeulenaere, M. Gontier, and A. J. Strazisar, "High resolution RANS nonlinear harmonic study of stage 67 tip injection physics," *J. Turbomach.* **137**(5), 051005 (2015).
- ³⁶M. Lange, M. Rolfes, R. Mailach, and H. Schräpp, "Periodic unsteady tip clearance vortex development in a low-speed axial research compressor at different tip clearances," *J. Turbomach.* **140**(3), 031005 (2018).
- ³⁷F. Wang and L. Di Mare, "Favre-averaged nonlinear harmonic method for compressible periodic flows," *AIAA J.* **57**(3), 1133–1142 (2019).
- ³⁸K. L. Suder, "Experimental investigation of the flow field in a transonic, axial flow compressor with respect to the development of blockage and loss," Ph.D. thesis (Case Western Reserve University, 1996).
- ³⁹K. Yamada, K. Funazaki, and H. Sasaki, "Numerical investigation of relation between unsteady behavior of tip leakage vortex and rotating disturbance in a transonic axial compressor rotor," ASME Paper No. GT2008-50779 (2008).
- ⁴⁰S. Vilmin, E. Lorrain, C. Hirsch, and M. Swoboda, "Unsteady flow modeling across the rotor/stator interface using the nonlinear harmonic method," ASME Paper No. GT2006-90210 (2006).
- ⁴¹G. A. Gerolymos, G. J. Michon, and J. Neubauer, "Analysis and application of chorochronic periodicity in turbomachinery rotor/stator interaction computations," *J. Propul. Power* **18**(6), 1139–1152 (2002).
- ⁴²D. Bruna and M. G. Turner, "Isothermal boundary condition at casing applied to the rotor 37 transonic axial flow compressor," *J. Turbomach.* **135**(3), 034501 (2013).
- ⁴³N. Qin, G. Carnie, Y. Wang, and S. Shahpar, "Design optimization of casing grooves using zipper layer meshing," *J. Turbomach.* **136**(3), 031002 (2014).
- ⁴⁴B. Cui, X. Wang, R. Wang, and Z. Xiao, "Numerical investigation of transonic axial compressor rotor flows using an improved transition-sensitized turbulence model," *Phys. Fluids* **33**, 035149 (2021).
- ⁴⁵A. Shabbir, M. L. Celestina, J. J. Adamczyk, and A. J. Strazisar, "The effect of hub leakage flow on two high speed axial flow compressor rotors," ASME Paper No. 97-GT-346 (1997).
- ⁴⁶K. L. Suder, "Blockage development in a transonic, axial compressor rotor," *J. Turbomach.* **120**(3), 465–476 (1998).
- ⁴⁷J. Park, "Optimal Latin-hypercube experiments," *J. Stat. Plann. Inference* **39**(1), 95–111 (1994).
- ⁴⁸K. Price, R. M. Storn, and J. A. Lampinen, *Differential Evolution: A Practical Approach to Global Optimization* (Springer, Heidelberg, Germany, 2005).
- ⁴⁹D. R. Jones, M. Schonlau, and W. J. Welch, "Efficient global optimization of expensive black-box functions," *J. Global Optim.* **13**, 455–492 (1998).
- ⁵⁰N. M. McDougall, N. A. Cumpsty, and T. P. Hynes, "Stall inception in axial flow compressors," *J. Turbomach.* **112**(1), 116–123 (1990).
- ⁵¹K. Yamada, K. Funazaki, and M. Furukawa, "The behavior of tip clearance flow at near-stall condition in a transonic axial compressor rotor," ASME Paper No. GT2007-27725 (2007).
- ⁵²C. Brandstetter, M. Jüngst, and H. P. Schiffer, "Measurements of radial vortices, spill forward, and vortex breakdown in a transonic compressor," *J. Turbomach.* **140**(6), 061004 (2018).
- ⁵³I. Wilke, H. P. Kau, and G. Brignole, "Numerically aided design of a high-efficient casing treatment for a transonic compressor," ASME Paper No. GT2005-68993 (2005).
- ⁵⁴B. H. Beheshti, B. Farhanieh, K. Ghorbanian, J. A. Teixeira, and P. C. Ivey, "Performance enhancement in transonic axial compressors using blade tip injection coupled with casing treatment," *Proc. Inst. Mech. Eng., Part A* **219**(5), 321–331 (2005).
- ⁵⁵B. H. Beheshti, K. Ghorbanian, B. Farhanieh, J. A. Teixeira, and P. C. Ivey, "A new design for tip injection in transonic axial compressors," ASME Paper No. GT2006-90007 (2006).
- ⁵⁶H. Khaleghi, M. A. S. Dehkordi, and A. M. Tousei, "Role of tip injection in desensitizing the compressor to the tip clearance size," *Aerosp. Sci. Technol.* **52**, 10–17 (2016).
- ⁵⁷W. Wang, W. Chu, and H. Zhang, "The effect of injector size on compressor performance in a transonic axial compressor with discrete tip injection," *Proc. Inst. Mech. Eng., Part A: J. Power Energy* **228**(7), 760–771 (2014).
- ⁵⁸M. Hoeger, G. Fritsch, and D. Bauer, "Numerical simulation of the shock-tip leakage vortex interaction in a HPC front stage," *J. Turbomach.* **121**(3), 456–468 (1999).
- ⁵⁹A. F. Mustaffa and V. Kanjirakkad, "Single and multiple circumferential casing groove for stall margin improvement in a transonic axial compressor," *J. Turbomach.* **143**(7), 071010 (2021).
- ⁶⁰D. E. Culley, M. M. Bright, P. S. Prahst, and A. J. Strazisar, "Active flow separation control of a stator vane using embedded injection in a multistage compressor experiment," *J. Turbomach.* **126**(1), 24–34 (2004).
- ⁶¹D. E. Van Zante, A. J. Strazisar, J. R. Wood, M. D. Hathaway, and T. H. Okiishi, "Recommendations for achieving accurate numerical simulation of tip clearance flows in transonic compressor rotors," *J. Turbomach.* **122**(4), 733–742 (2000).
- ⁶²J. Hou, Y. Liu, L. Zhong, W. Zhong, and Y. Tang, "Effect of vorticity transport on flow structure in the tip region of axial compressors," *Phys. Fluids* **34**, 055102 (2022).
- ⁶³X. He, Z. Fang, G. Rigas, and M. Vahdati, "Spectral proper orthogonal decomposition of compressor tip leakage flow," *Phys. Fluids* **33**, 105105 (2021).